BNL-222007-2021-JAAM

Atomically dispersed single iron sites for promoting Pt and Pt3Co fuel cell catalysts: performance and durability improvements

Z. Qiao, S. Hwang

To be published in "Energy & Environmental Science"

July 2021

Center for Functional Nanomaterials

Brookhaven National Laboratory

U.S. Department of Energy

USDOE Office of Science (SC), Basic Energy Sciences (BES) (SC-22)

This is the author's manuscript of the article published in final edited form as:

Qiao, Z., Wang, C., Li, C., Zeng, Y., Hwang, S., Li, B., Karakalos, S., Park, J., Kropf, A. J., Wegener, E. C., Gong, Q., Xu, H., Wang, G., Myers, D. J., Xie, J., Spendelow, J. S., & Wu, G. (2021). Atomically dispersed single iron sites for promoting Pt and Pt3Co fuel cell catalysts: Performance and durability improvements. Energy & Environmental Science, 14(9), 4948–4960. https://doi.org/10.1039/D1EE01675J

DISCLAIMER

Atomically Dispersed Single Iron Sites for Promoting Pt and Pt_3Co Fuel Cell Catalysts: Performance and Durability Improvements

Zhi Qiao[1,+], Chenyu Wang[2,+], Chenzhao Li[3,+], Yachao Zeng[1,+], Sooyeon Hwang[4,*], Boyang Li[5], Stavros Karakalos[6], Jaehyung Park[7], A. Jeremy Kropf[7], Evan C. Wegener[7], Qing Gong[3], Hui Xu[8], Guofeng Wang[5], Deborah J. Myers[7,*], Jian Xie[3,*], Jacob S Spendelow[2,*], and Gang Wu[1,*]

[1] Department of Chemical and Biological Engineering, University at Buffalo, The State University of New York, Buffalo, New York 14260, USA. E-mail: gangwu@buffalo.edu

[2] Materials Physics and Applications Division, Los Alamos National Laboratory, Los Alamos, NM, 87545 USA, E-mail: spendelow@lanl.gov

[3] Department of Mechanical Engineering, Purdue School of Engineering and Technology, Indiana University-Purdue University, Indianapolis, Indiana 46202, USA. Email: jiaxie@iupui.edu

[4] Center for Functional Nanomaterials, Brookhaven National Laboratory, Upton, New York 11973, United States. E-mail soohwang@bnl.gov

[5] Department of Mechanical Engineering and Materials Science, University of Pittsburgh, Pittsburgh, PA 15261, United States.

[6] Department of Chemical Engineering, University of South Carolina, Columbia, South Carolina 29208, United States

[7] Chemical Sciences and Engineering Division, Argonne National Laboratory, Lemont, IL 60439, United States. E-mail: dmyers@anl.gov

[8]Giner Inc., Newton, Massachusetts 02466, United States

+ These authors contributed equally

TOC

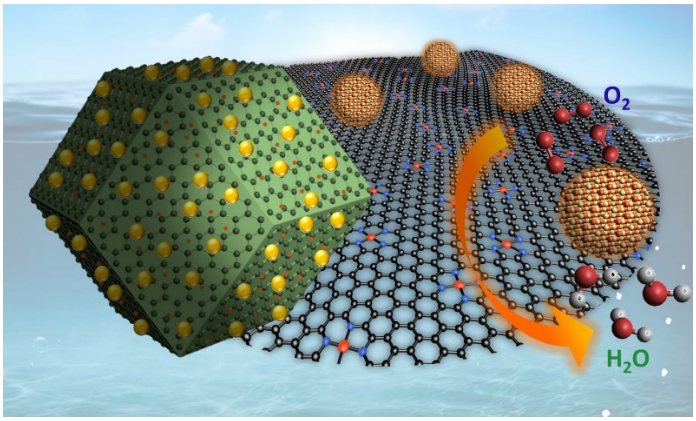

Broader Context

Fuel cell electric vehicles (FCV) are considered the most promising and utmost solution for electric transportation. The membrane electrode assembly (MEA) is the key component in fuel cells, governing their cost, performance, and durability. A successful MEA for heavy-duty vehicles should have >65% energy efficiency and 25,000 hour durability while limiting the platinum group metal (PGM) loading to 0.3 mg/cm^2. One of the critical issues of current MEAs is the lack of highly active and stable catalysts to efficiently catalyze the kinetically sluggish oxygen reduction reaction (ORR) at the cathode. Carbon-supported PtCo alloy nanoparticles are the typical PGM catalysts used for commercial fuel cell vehicles. High PGM loadings are required to mitigate their fast degradation. Alternatively, the atomically dispersed Fe-N-C catalysts have become the most promising PGM-free catalysts, but have not fully succeeded yet due to their unsatisfactory long-term durability. Here, we discovered a possible synergy between PGM and PGM-free active sites and developed an effective strategy to integrate them into one catalyst, showing significantly enhanced MEA performance and durability while reducing PGM loading. The approach provides a new opportunity to design advanced catalysts for FCVs and explore possible synergy among different active sites for critical electrocatalysis processes.

Abstract: Significantly reducing platinum group metal (PGM) loading while improving catalytic performance and durability is critical to accelerating proton-exchange membrane fuel cells

(PEMFCs) for transportation. Here we report an effective strategy to boost PGM catalysts through integrating PGM-free atomically-dispersed single metal active sites in the carbon support toward the cathode oxygen reduction reaction (ORR). We achieved uniform and fine Pt nanoparticle (NP) (~2 nm) dispersion on an already highly ORR-active FeN_4 site-rich carbon support (FeN_4-C). Furthermore, we discovered an effective approach to preparing a well-dispersed and highly ordered $L1_2$ Pt_3Co intermetallic nanoparticle catalyst on the FeN_4-C support. DFT calculations predicted a synergistic interaction between Pt clusters and surrounding FeN_4 sites through weakening O_2 adsorption by 0.15 eV on Pt sites, thereby enhancing the intrinsic activity of Pt. Experimentally, we verified the synergistic effect between Pt or Pt_3Co NPs and FeN_4 sites, leading to significantly enhanced ORR activity and stability. Especially in a membrane electrode assembly (MEA) with a low cathode Pt loading (0.1 $mgPt/cm^2$), the Pt/FeN_4-C catalyst without alloying achieved a mass activity of 0.451 A/mg_{Pt} and retained 80% of the initial values after 30,000 voltage cycles (0.6 to 0.95 V), exceeding DOE 2020 targets. Furthermore, the Pt_3Co/FeN_4 catalyst achieved significantly enhanced performance and durability concerning initial mass activity (0.72 and A/mg_{Pt}), power density (824 mW/cm^2 at 0.67 V), and stability (23 mV loss at 1.0 A $/cm^2$). The approach to exploring the synergy between Pt and Fe-N-C catalysts provides a new opportunity to design advanced catalysts for various electrocatalysis processes.

1. Introduction

Effective and durable catalysts are desperately demanded to minimize electrochemical activation overpotentials for the oxygen reduction reaction (ORR) cathode to promote energy conversion efficiency in proton-exchange membrane fuel cells (PEMFCs) for transportation. Platinum (Pt) is the only metal catalyst showing promising performance and durability in challenging acidic

media.[1-3] Unfortunately, the high cost and scarcity of Pt limit the large-scale deployment of fuel cell electric vehicles (FCV), which has driven intensive efforts to reduce Pt content in ORR catalysts via two approaches.[4, 5] The first strategy is to alloy Pt with a first-row transition metal (M), such as Co,[6, 7] Ni,[8-12] and Fe.[13, 14] With a smaller atomic radius, incorporating M atoms in the Pt-based alloy brings beneficial strain and alloy effects that are significant to weaken O_2/intermediates adsorption and improve intrinsic ORR activity.[15, 16] Although some PtNi alloy catalysts exhibited higher intrinsic activity than others,[8, 17] they are not stable during the ORR and suffer from severe activity degradation due to the possible phase separation. Therefore, PtCo alloys are currently the most promising system to design advanced fuel cell catalysts.[18]

Compared to the common solid solution A1-structure, certain PtCo alloys with specific Pt/Co compositions can form ordered intermetallic structures, including the cubic $L1_2$ (Pt_3Co) or the tetragonal $L1_0$ (PtCo). The ordered intermetallic structure is attributed to the negative enthalpy change often derived from a strong 3d-5d orbital interaction between Co and Pt, which enables stabilization of Co.[19] Compared to traditional fcc Pt alloys, the ordered intermetallic structure results in less M leaching and improved stability under acidic fuel cell conditions.[20, 21] Unlike the disordered A1-structure, the cubic $L1_2$ and the tetragonal $L1_0$ structures usually are obtained by thermal annealing at high temperatures (>700°C). However, nanoparticle (NP) agglomeration at such high temperatures results in large particle sizes, which cannot provide adequate electrochemically active surface areas (ECSAs) for high catalytic mass activity.[19] Therefore, preparing highly ordered PtCo intermetallic NPs while maintaining sufficiently fine particle sizes remains a grand challenge.[21]

Another approach is to develop platinum group metal (PGM)-free catalysts. Currently, the most promising PGM-free catalysts are atomically dispersed metal (M: Fe and Co) single sites

coordinated with nitrogen and embedded in carbon (M-N-C).[22-26] The most promising M-N-C catalysts are derived from Fe and zeolitic imidazolate framework-8 (ZIF-8) precursors, demonstrating encouraging ORR activity approaching Pt catalysts.[27-29] The nitrogen coordinated single metal sites (*i.e.*, FeN_4) are believed the ORR active sites and atomically dispersed throughout the carbon. However, their insufficient long-term stability (up to 5000 hours) under PEMFC operations is a fatal drawback, placing the development of PGM-free catalysts as high-risk research.[30] Nevertheless, such an active carbon-based Fe-N-C catalyst could be desirable to disperse Pt or Pt alloy NPs, providing additional PGM-free active sites to reduce Pt loading in the ORR cathode. Furthermore, the dominant N dopants and porosity in the Fe-N-C carbon support could stabilize Pt NPs with strengthened metal-support interactions.[31, 32] Importantly, the possible synergy between Pt and atomically dispersed MN_4 sites could further lead to performance enhancement.[33, 34] Recently, we have developed a new class of highly active Fe-N-C catalyst, consisting of atomically dispersed FeN_4 sites (0.5 at.% Fe) embedded in carbon (96 at.%).[28] In addition to the compelling ORR activity in the acidic electrolyte (half-wave potential $E_{1/2}$ =0.87 V),[27, 28] its hierarchical pore structure, high surface area, adjustable particle sizes, and nitrogen dopants (3-4 at%) are the essential features in carbon supports for Pt and PtCo alloy catalysts.

Here, we report an effective approach to designing hybrid ORR catalysts by integrating PGM NPs and the FeN_4 site-rich Fe-N-C carbon denoted as Pt/FeN_4-C or PtCo/FeN_4-C. A Fe-free nitrogen-doped carbon (NC) and a CoN_4-C support derived from ZIF-8 and cobalt-doped ZIF-8 precursors, respectively, were also studied. The aim is to justify the effectiveness of FeN_4 sites in carbon to dramatically enhance Pt and PtCo catalyst performance. Furthermore, during the synthesis of PtCo/FeN_4-C catalysts, we developed an effective approach to preparing $L1_2$ Pt_3Co intermetallic structures through controlled high-temperature annealing treatments. The favorable

porous carbon structure and abundant nitrogen dopants in the FeN_4-C enable a uniform and fine Pt and Pt_3Co NP distribution. Unlike large particle sizes of ordered PtCo intermetallic reported before, the use of the FeN_4 site-rich Fe-N-C carbon can effectively retain a desirable particle size (3-4 nm) while achieving an ordered structure during a high-temperature annealing treatment. The Pt/FeN_4-C and Pt-Co/FeN_4-C catalysts show excellent performance and durability in rotating disk electrode (RDE) and membrane electrode assembly (MEA) studies. Unlike traditional carbon black-supported Pt (Pt/C), the Pt/FeN_4-C-based MEA with a low cathode loading of 0.1 mg_{Pt}/cm^2 achieved significantly improved ORR mass activity (MA) of 0.451 A/mg_{Pt} and retained 80% of the initial value after 30,000 voltage cycles during the catalyst accelerated stress test (AST), exceeding the DOE 2020 targets even without using an alloy. Furthermore, the Pt_3Co/FeN_4-C-based MEA with the same Pt loading achieved much higher ORR mass activities of 0.72 A/mg_{Pt}. The Pt_3Co/FeN_4 catalyst reached a power density of 824 mW/cm^2 at 0.67 V and only lost 23 mV at 1.0 A $/cm^2$ after the standard catalyst AST (30,000 cycles). DFT calculations further elucidated the possible synergistic mechanism between Pt and FeN_4 sites in terms of the enhanced intrinsic activity of Pt due to weakened O_2 adsorption energy and reduced activation energy to break O-O bonds during the ORR. The promotional role of the FeN_4 site in boosting the activity and stability of Pt catalysts presented an effective strategy to design high-performance low-PGM catalysts and electrodes in PEMFCs for transportation.

2. Results and Discussion

2.1. Catalysts Synthesis and Structures

We have developed promising Fe-N-C catalysts containing highly active FeN_4 sites through multiple effective methods.[35] Here, we used a chemical doping of Fe^{3+} ions into ZIF-8 nanocrystals and partially replaced Zn to form Fe-N_4 coordination followed by subsequent pyrolysis in an Ar

atmosphere to convert the Fe-doped ZIF-8 to FeN_4 active sites uniformly dispersed into partially graphitized carbon.[28] The carbon phase, derived from the hydrocarbon in ZIF-8, is partially graphitized and has a surface area up to 700 m^2/g, containing atomically dispersed FeN_4 sites with a significant micropore volume connected to hierarchical porous structures. More importantly, the carbon particle size can be easily tuned during the synthesis, ranging from 20 to 1000 nm,[27] which provides an excellent opportunity to design electrode structures in MEAs. Therefore, we applied the FeN_4 site-rich carbon (FeN_4-C) to synthesize Pt and PtCo catalysts. The degree of the graphitization of carbon support is critical to Pt catalyst stability.[36] Thus, unlike traditional Fe-N-C catalysts with significant amorphous carbon, we further prolonged the pyrolysis duration from one to three hours at 1100 ºC to graphitize the FeN_4-C, aiming to increase catalyst stability. The graphitized layer structure of the FeN_4-C is apparent in the corresponding STEM images (**Figure S1a** and **S2)** and further verified from a sharp (002) peak in XRD patterns and well-separated D (~1339 cm^{-1}) and G (~1589 cm^{-1}) peaks along with the appearance of a 2D (~2700 cm^{-1}) peak in Raman spectra (**Figure S1b** and **S3**). The high ORR activity of the FeN_4-C is confirmed with an $E_{1/2}$ of 0.87 V *vs*. RHE in RDE testing under the conditions of 0.6 mg/cm^2 loading, 900 rpm, and 25 ºC in 0.5 M H_2SO_4. The abundant and uniform distribution of nitrogen dopants and single Fe sites are throughout the FeN_4-C shown in mapping images (**Figure S4**). Therefore, the nitrogen species are well preserved in the carbon even after a prolonged pyrolysis, corresponding to its high ORR activity.[37]

During the subsequent Pt deposition, we developed an impregnation method with freeze-drying to disperse Pt NPs on the FeN_4-C support. A forming gas (5% H_2 in Ar) was applied as a reductant at 200 ºC to prepare the Pt/FeN_4-C catalyst. This method minimizes the possible damage of FeN_4 sites by avoiding a complicated wet chemistry synthesis.[38] This catalyst synthesis scheme

is illustrated in **Figures 1a** and **1b.** Atomically dispersed FeN_4 sites, shown as single bright spots **(Figure S1a)**, can be observed in the FeN_4-C carbon support. After the Pt deposition, Pt NPs with a uniform particle size around 2.4 nm (**Figure 1d** and **S5a**) co-exist with FeN_4 sites embedded in carbon (**Figure 1c** and **1e**). These isolated single metal sites are identified to co-exist with N at the atomic level (**Figure 1e** and **f**) verified using electron energy-loss spectroscopy (EELS). This is a typical feature of atomically dispersed single Fe site catalysts, likely in FeN_4 active sites.[28, 29, 39-41] These atomic FeN_4 sites are abundant and can be clearly distinguished in the carbon support with uniform dispersion (**Figure S6**). The STEM-EDX mapping of the Pt/FeN_4-C in **Figure S7** showed relatively separate existence of Pt and Fe with a small portion of Fe sites around the Pt NPs. Fe-based aggregates were not observed in the catalyst.

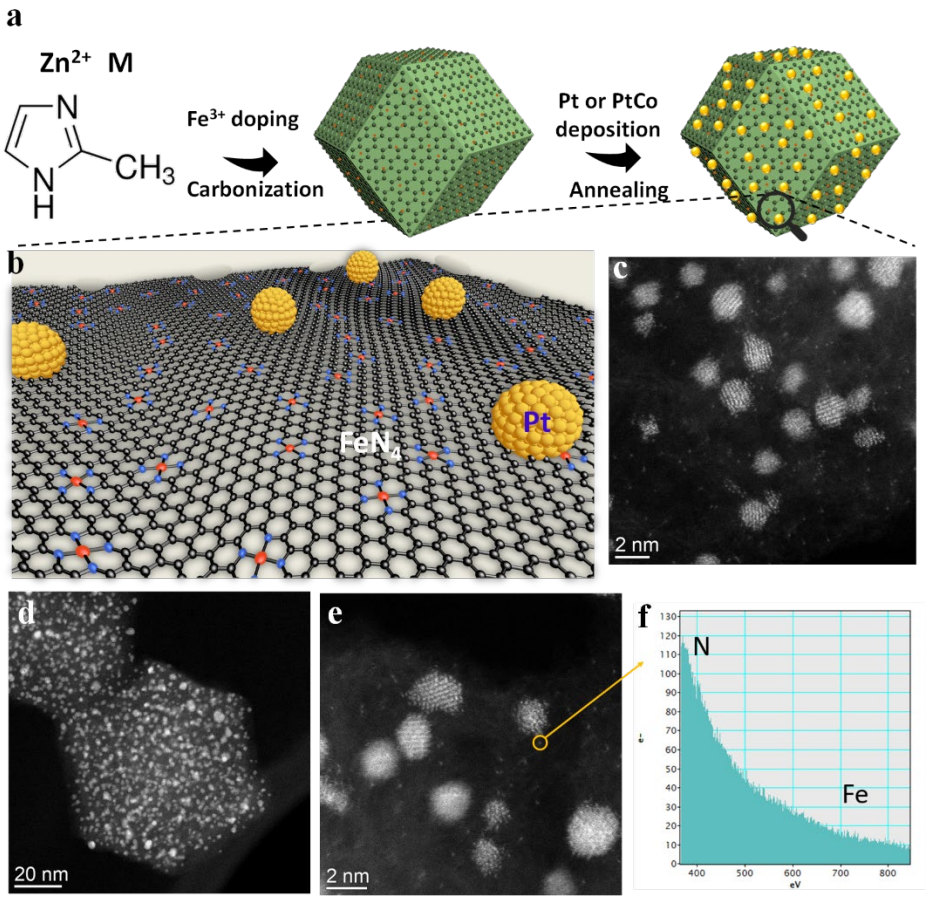

Figure 1. (**a**)**.** A synthesis scheme of this FeN_4-C derived carbon-supported Pt or PtCo catalysts. (**b**). Schematics of Pt/FeN_4-C (Pt-Co/FeN_4-C) catalysts, showing coexistence of Pt-based NPs and FeN_4 PGM-free active sites. (**c-e)** STEM images of the Pt/FeN_4-C catalyst showing the uniform distribution of Pt nanoparticles and the coexistence with FeN_4 sites (**f**) EELS analysis of the elemental composition were provided for the circled little bright spots in (**e**).

PtCo intermetallic NP catalysts represent one of the most active ORR catalysts.[18] Recent work on intermetallic PtCo NPs has demonstrated that two types of intermetallic ordered structures (*i.e.*, $L1_0$ PtCo and $L1_2$ Pt_3Co) can improve the performance and durability.[4, 7, 21, 34] We discovered that the atmosphere employed during the annealing could control the obtained intermetallic ordered structures. The Ar flow is favorable for $L1_2$ Pt_3Co, while the forming gas assists the formation of $L1_0$ PtCo (**Figure 2a)**. However, the $L1_2$ Pt_3Co catalyst exhibited enhanced MEA performance and similar durability compared to the $L1_0$ PtCo. Here, we only reported the relevant results for the $L1_2$ Pt_3Co catalyst. Therefore, we integrated Pt_3Co intermetallic NPs with the active FeN_4-C support using an impregnation method followed by a reduction under forming gas at 200 ºC. Then, we performed second-step annealing at 650°C under Ar atmosphere to prepare the $L1_2$ (Pt_3Co) intermetallic structure, which was confirmed using XRD (**Figure 2b)**. Excess Co could behave as an obstacle to the formation of NP agglomerates during the annealing and can be easily removed using subsequent acid treatment. This new method enables effective control of $L1_2$ (Pt_3Co) intermetallic structures on the FeN_4-C support with a fine particle dispersion.

High-angle annular dark-field scanning transmission electron microscopy (HAADF-STEM) was used to further study the structures of Pt_3Co NPs. Significant atomic number difference between Co (Z = 27) and Pt (Z = 78) enables clear visualization of atomic ordering in bimetallic Pt-Co NPs through the atomic number (Z) contrast imaging.[42] **Figure 2c** shows a typical $L1_2$ Pt_3Co NP viewed along the (001) direction, exhibiting face-centered cubic crystal structure

with Pt: Co in a 3:1 ratio. Pt shell structures for the Pt_3Co catalysts are apparent after an acid leaching process, demonstrating a structure known to be highly active for the ORR.[6] Pt_3Co NPs are surrounded by FeN_4 sites at the atomic scale (**Figure 2d)**, indicating their close location for a possible synergistic effect to boost the ORR. In a STEM image with low magnification, $L1_2$ Pt-Co NPs with an average particle size of 4.2 nm are uniformly dispersed on the FeN_4-C carbon support. (**Figure 2e** and **S5**). We speculate that the small particle sizes with narrow distribution result from the favorable porous structure and abundant FeN_4 sites in the carbon support (**Figure S8**), generating electronic confinement effects on Pt-Co NPs and restraining their particle agglomeration during the annealing.[43]

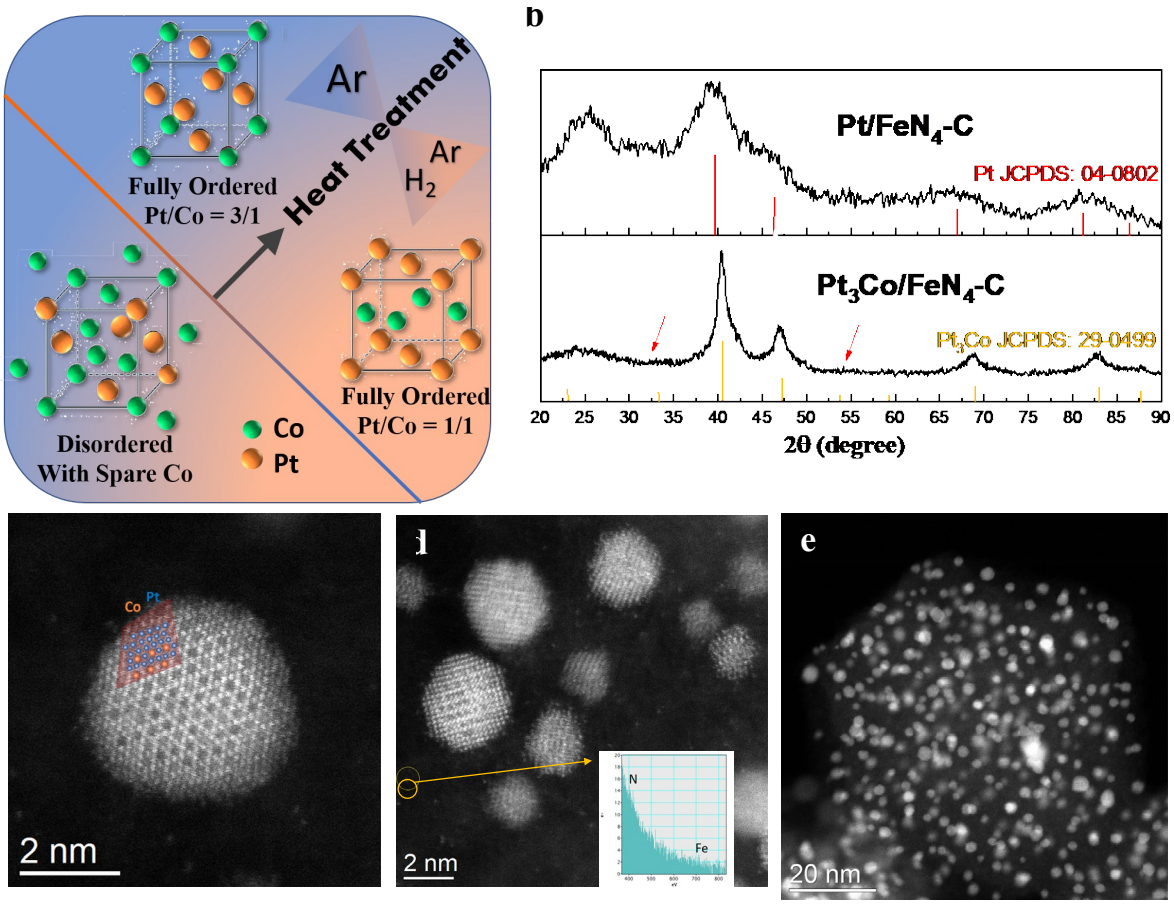

Figure 2. (**a)** Illustration of $Pt_3Co(L1_2)$ intermetallic structures synthesis. (**b)** XRD spectra of two different catalysts. The STEM image of a Pt_3Co/FeN_4-C NP showing the corresponding core-shell

ordering structures and NPs distribution (**c**). The HAADF-STEM image of the Pt_3Co/FeN_4-C catalyst showing the coexistence of intermetallic NPs and FeN_4 sites and the EELS analysis of the elemental composition were provided for the circled small bright spot in the (**d**). The STEM image shows uniform Pt3Co NP dispersion with an average size of 4.2 nm on the FeN4-C support (**e**).

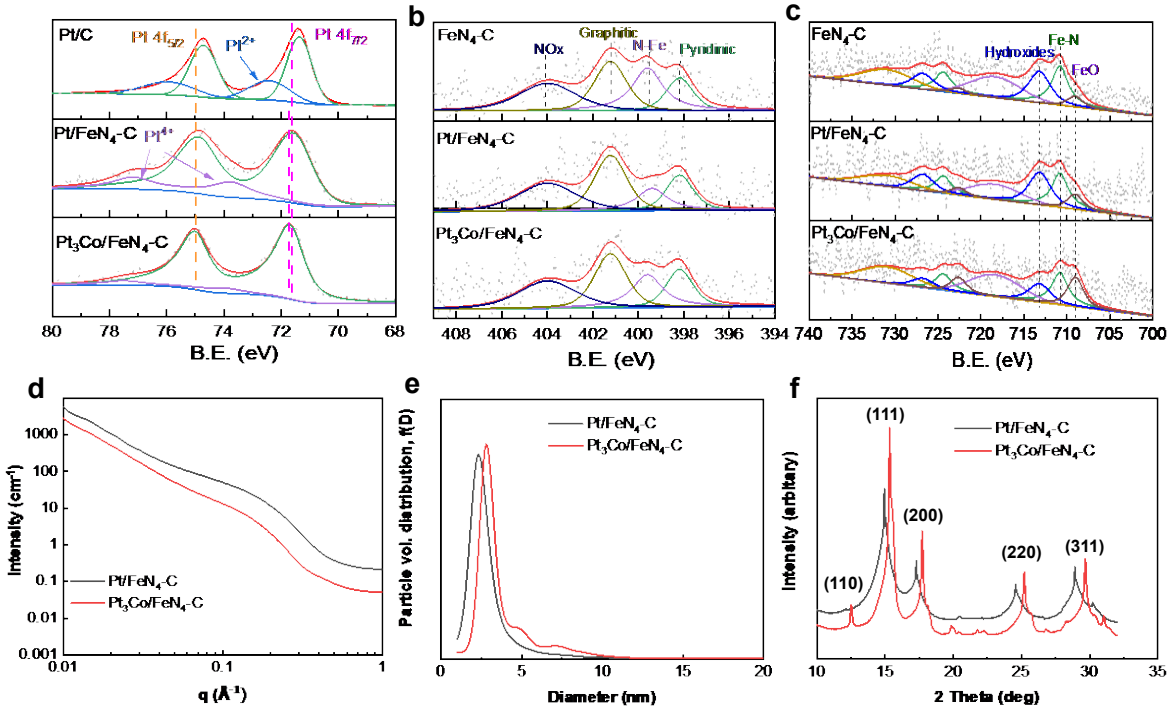

Figure 3. X-ray photoelectron spectroscopy analysis of (**a**) Pt 4f, (**b**) N 1s, and (**c**) Fe 2p for various studied Pt-based catalysts. (**d**). X-ray scattering curves in the small-angle (SAXS) region, (**e**). Metal particle volume distributions obtained from SAXS data fits, and (**f**). Wide-angle X-ray scattering (WAXS) curves for the Pt/FeN_4-C and the Pt_3Co/FeN_4-C.

We also investigated the FeN_4-C supported Pt and Pt_3Co catalysts' electronic structures using X-ray photoelectron spectroscopy (XPS). Possible electron transfer from Pt to the FeN_4-C support causes a positive shift in the Pt 4f binding energy in the Pt/FeN_4-C catalyst (**Figure 3a**) compared to conventional Pt/C. FeN_4 sites embedded carbon, behaving electronegatively, can modify the electronic structure of adjacent carbon. The resultant electron deficiency of carbon

likely strengthens the Pt NP deposition and enhances the metal-support interactions.[36, 44] The similar strengthening effect was observed for the Pt_3Co intermetallic NP, evidenced by a further positive shift of Pt 4f binding energy than the Pt/FeN_4-C. Due to the incorporation of Co, these positive shifts of Pt 4f binding energy could be partially caused by the interaction among Pt and Co, along with the introduced strain effects.[45 34, 46, 47] Metallic Co^0 has a high content than Co^{2+} species in the Pt_3Co/FeN_4-C (**Figure S9**). In addition, abundant nitrogen defects in the carbon support may coordinate with Co species during the annealing process.[48-51] As for the N 1s XPS, both Pt and Pt-Co catalysts demonstrated abundant pyridinic N (398.6 eV), graphitic N (401.1 eV), and the possible Fe-N (399.6 eV) content, which is consistent with the FeN_4-C support (**Figure 3b**). Pyridinic N and Fe-N bonds are generally evidenced to be the formation of FeN_4 active sites (**Figure 3c**), indicating that the FeN_4 active sites in supports are well preserved for all the corresponding Pt or Pt_3Co catalysts consistent with the STEM images.

The small-angle X-ray scattering (SAXS) regions of the X-ray scattering curves are shown in **Figure 3d**. The most prominent feature of these curves is the scattering feature in the 0.04 to 0.6 $Å^{-1}$ region, attributed to scattering from metal particles. The scattering in this region was fit to yield the particle size distributions shown in **Figure 3e**. These data show that as-prepared catalysts have narrow and substantially mono-modal particle size distributions with mean diameters less than 2 nm. The wide-angle X-ray scattering (WAXS) regions of the X-ray scattering curves are shown in **Figure 3f**. The WAXS curves show peaks attributed to scattering from the (111), (200), (220), and (311) planes. As illustrated in Figure 3f, incorporating Co into the catalyst causes a shift of all scattering peaks to larger two-theta values relative to the scattering peaks observed for the Pt/FeN_4-C indicative of lattice compression due to the incorporation of smaller Co atoms. Also evident in Figure 3f is scattering from the (110) plane indicative of the presence of the $L1_2$ Pt_3Co

ordered intermetallic phase.[52] As discussed by Xiong et al.,[52] the ratio of the area of the (110) peak to the sum of the areas of the (111) and (200) peaks can be used to estimate the volume fraction of Pt_3Co comprising the ordered intermetallic phase versus the solid solution phase. This calculation for the peak areas of the Pt_3Co/FeN_4-C catalyst (Figure 3f) and comparison with the plot of $I_{110}/(I_{111}+I_{200})$[53] indicates that approximately 25% of the Pt_3Co is in the $L1_2$ phase. Further optimizing Pt: Co ratios and the annealing temperature and duration is critical to increasing ordered structures for enhanced catalytic activity and stability.

2.2. ORR activity and stability in aqueous acidic electrolytes

We evaluated the ORR activity and stability of FeN_4-C supported Pt and Pt_3Co catalysts in 0.1 M $HClO_4$ electrolyte using the RRDE method (**Figure 4a)**. The Pt weight fraction (20 wt.%) in both Pt and Pt_3Co catalysts was verified by using thermogravimetric analysis (TGA) to accurately determine the Pt loading during electrochemical measurements (**Figure S10**). The Pt/FeN_4-C catalyst showed enhanced performance with an $E_{1/2}$ of 0.9 V *vs*. RHE (60 $\mu g_{Pt}/cm^2$, 1600 rpm, 25 ^oC, and 0.1 M $HClO_4$) and mass activity (MA) of 0.57 A/mg_{Pt} at 0.9 V vs. RHE, superior to a commercial Pt/Vulcan Carbon (Pt/C) catalysts (TEC10V20E from TKK) ($E_{1/2}$: 0.87 V and 0.242 A/mg_{Pt}). Hence, the enhanced activity suggested that the FeN_4 active sites in the support may promote the Pt/FeN_4-C catalyst due to either mass or intrinsic activity improvements or both. Furthermore, the Pt_3Co/FeN_4-C catalyst exhibited outstanding catalytic activity with $E_{1/2}$ of around 0.95 V *vs*. RHE. Notably, unlike the Pt_3Co/FeN_4-C catalyst, additional acidic treatment cannot further enhance the activity of the Pt/FeN_4-C catalyst. Although the Pt/FeN_4-C catalyst exhibited higher electrochemically-active surface area ECSA (72.2 m^2/g) than the Pt/C (55.1 m^2/g) and Pt_3Co catalysts (49.7 m^2/g) (**Figure 4b**), the Pt_3Co/FeN_4-C catalyst is more active due to the high intrinsic activity of Pt_3Co vs. Pt. A similar trend was also observed in other studies,[54] showing

PtM/C catalysts often exhibit relatively lower ECSA value but much-enhanced activity relative to Pt/C catalysts.

Figure 4c compares the measured specific activities (SA) and MA for the Pt_3Co/FeN_4-C (SA 3.98 mA/cm^2_{Pt}; MA: 1.34 $mA/\mu g_{Pt}$), representing one of the most active PGM catalysts.[4] We employed the underpotential hydrogen adsorption/desorption (HAD) reaction using cyclic voltammetry to determine ECSA rather than CO stripping experiments. However, it may underestimate the real ECSA by the factor of 1.5 due to the suppression in HAD on small Pt NPs (2-3 nm) of these catalysts primarily attributed to the changes in surface-structure-sensitive adsorption caused by a possible ensemble effect.[55] Both the Pt/FeN_4-C and Pt_3Co/FeN_4-C catalyst showed an insignificant yield of H_2O_2 below 0.25% at the full potential range (**Figure S11**). Thus, the four-electron pathway is dominant on these studied Pt and Pt_3Co catalysts during the ORR.

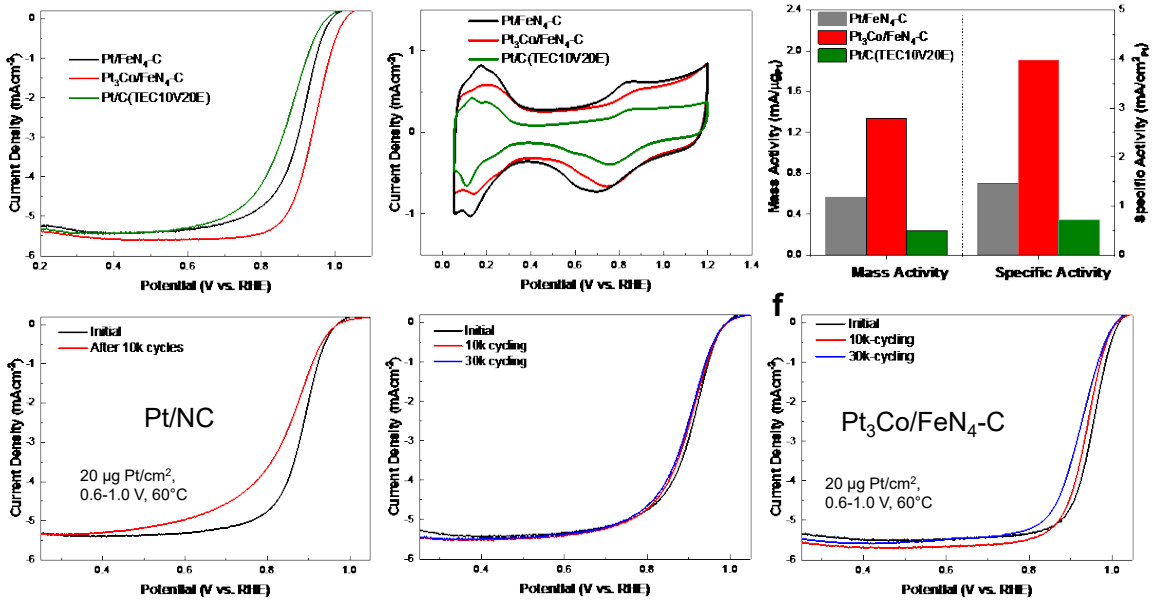

Figure 4. (a) ORR polarization plots for FeN_4-C supported Pt and Pt_3Co catalysts and commercial Pt/C catalyst. (**b)** The corresponding CV plots and the corresponding ECSA, and (**c)** the corresponding mass activities and specific activities at 0.9 V after IR correction. RDE potential

cycling stability tests for (**d)** the Pt/NC, (**e)** the Pt/FeN_4-C, and (**f)** the Pt_3Co/FeN_4-C catalysts in the potential range of 0.6–1.0 V.

The stability for all studied catalysts was evaluated in an acidic electrolyte using RDE. Compared to a Pt/C catalyst (TEC10V20E) (**Figure 4d**), the Pt/FeN_4-C catalyst exhibited superior stability during accelerated stress tests (ASTs) under 30000 potential cycles from 0.6 to 1.0 V at 60ºC (**Figure 4e**). Besides FeN_4 active sites, atomically-dispersed CoN_4 sites and metal-free N-doped carbon are also identified as promising PGM-free catalyst supports.[50, 51] Compared with the Pt/CoN_4-C and the Pt/NC, the Pt/Fe_4N-C exhibited enhanced catalytic activity. Most importantly, unlike the apparent activity loss observed with the Pt/CoN_4 and the Pt/NC catalysts, there is almost no decline for the Pt/FeN_4-C after the AST (**Figure S12**). The enhanced stability is likely due to the strengthened metal-support interactions originating from abundant FeN_4 sites in the highly graphitized carbon (**Figure S13)**. Also, the change of double-layer capacitance (0.4 to 0.6 V) for the Pt/FeN_4-C catalyst after the long-term AST in RDE is insignificant (**Figure S14)**, indicating the robust carbon structure of the Pt/FeN_4-C catalyst. Although the Pt_3Co/FeN_4-C presents outstanding activity, its degradation of around 30 mV in $E_{1/2}$ was observed during the AST stability at 60 °C in 0.1 M $HClO_4$ electrolyte (**Figure 4f**). In agreement with Pt catalysts, the FeN_4-C-supported PtCo catalysts showed enhanced stability relative to the CoN_4-C and NC-supported catalysts (**Figure S15)**, further confirming the strong interaction provided by FeN_4 active sites in the carbon.

2.3. MEA Tests in Fuel Cells

We further evaluated the catalyst performance in fuel cell environments, which involves incorporating the catalyst with solid-state ionomer for proton-conduction and the formation of

porous electrode structures. We tested different FeN_4-C-supported Pt and Pt_3Co catalysts as the cathode in MEAs (Pt loadings at the anode and cathode are 0.1 mg_{Pt}/cm^2) under H_2-air (**Figure 5**) by using a 5 cm^2 differential cells containing 14 parallel flow channels. Our previous MEA studies on PGM-free catalysts indicated that the particle size of FeN_4-C carbon significantly affects the catalyst MEA performance.[56] Therefore, we deposited Pt NPs onto FeN_4-C carbon supports with various sizes of 50, 100, and 200 nm, and evaluated their MEA performances. Results shown in **Figure 5a** indicate that the 100 nm FeN_4-C supported Pt catalyst significantly outperforms the others, achieving a much higher current density throughout the entire voltage range. The performance differences may be attributed to the corresponding ionomer dispersion and mass transport limitation in different pore structures resulting from different primary carbon particle sizes (**Figure S16 and Table S1**). Our previous studies using nano-CT imaging on PGM-free Fe-N-C catalysts indicated that the 100 nm carbon particle size leads to uniform ionomer dispersion with the least proton resistance.[56]

Based on the optimal 100 nm FeN_4-C support, we compared the MEA performance of the Pt/FeN_4-C and the Pt_3Co/FeN_4-C catalysts with a commercial Pt/C catalyst, as shown in **Figure 5b**. The Pt/FeN_4-C demonstrated a much higher current density than the commercial Pt/C in the typical operating voltage range (>0.6 V). The corresponding MEA generated a MA at 0.9 V of 0.45 A/mg_{Pt} exceeding the DOE target of 0.44 mA/mg_{Pt} even without using PtM alloys. The generated current densities at 0.67 V (1.02 A/cm^2) and 0.80 V (0. 252 A/cm^2) are much higher than the Pt/Vulcan (0.77 A/cm^2 at 0.67 V and 0.10 A/cm^2 at 0.80 V). The newly achieved MEA performance using the Pt/FeN_4 cathode catalyst is exceptional, comparable with most of the Pt alloy catalysts published.[7, 20] Notably, the much-enhanced mass activity at 0.9 V may not be directly contributed by the FeN_4 active sites in the support. However, the synergistic effect

originating from FeN_4 may boost the intrinsic activity of Pt sites, as discussed in the following section in detail.

In good agreement with RDE tests in acidic electrolytes, the Pt_3Co/FeN_4-C catalyst performs much better in MEAs than the Pt/FeN_4-C catalyst. The Pt_3Co/FeN_4-C cathode exhibited excellent MA at 0.9 V of 0.72 A/mg_{Pt} relative to the DOE target (0.440 mA/mg_{Pt}). The Pt_3Co/FeN_4-C catalysts generated 0.355 A/cm^2 at 0.8 V, exceeding the DOE target of 300 mA/cm^2. At the critical voltage of 0.67 V, the MEA yielded 1.23 A/cm^2, corresponding to power densities of 824 mW/cm^2. However, compared with the commercial Pt/C catalysts, these FeN_4-C supported Pt and Pt_3Co catalysts exhibited lower performance at a high current density range. The large volume of micropores in the ZIF-8 derived carbon structure is likely flooded by water, causing mass transport limitations. Increasing mesopore with optimal hydrophobicity for the FeN_4-C support is crucial for mitigating water flooding and improving performance.

These Pt and PtCo catalysts were also subjected to AST for 30000 voltage cycles from 0.6 to 0.95 V with a 0.5 s rise time and 2.5 s dwell time at each potential under H_2/N_2 atmosphere. Compared to the Pt/C with 127 mV loss (**Figures 5c),** the Pt/FeN_4-C exhibited superior stability during AST, with only 5 mV loss at 1.0 A/cm^2 and 20% loss in MA at 0.9 V (**Figure 5d**), significantly exceeding the DOE targets of 30 mV and 40% MA loss. Likewise, the Pt_3Co/FeN_4-C catalyst displayed good stability in the MEA with corresponding voltage losses of 23 mV at 1.0 A/cm^2 and 21 mV at 0.8 A/cm^2, exceeding the DOE stability target (30 mV loss) (**Figure 5e**). Unlike the RDE results at 60°C, the Pt_3Co/FeN_4-C MEA exhibited slightly better stability concerning mass activity loss at 0.9 V (from 0.72 to 0.44 A/mg_{Pt}, -38%). This is possibly due to the relatively larger particle size of Pt_3Co NPs, which are more stable in the fuel cell operating environment. For comparison, MAs and H_2-air MEA durability for the Pt_3Co/FeN_4-C and the

Pt/FeN_4-C catalyst are provided in **Figure 5f** and **Table S2**. Generally, Pt-based alloy exhibited higher activity but inferior stability compared to individual Pt catalysts due to the possible M leaching and the reconstruction of surface alloy structures. Engineering the particle size for an optimal activity-stability tradeoff is critical to the Pt_3Co/FeN_4-C catalyst by extending the annealing duration or slightly increase the heating temperature for further enhanced durability. In addition, a robust Pt-shell for Pt_3Co particles is also believed to mitigate the Co leaching,[57] which can be realized by applying an acidic treatment followed by an annealing treatment. Further increasing the ordered degree of Pt_3Co intermetallic particles is also critical for enhanced stability.

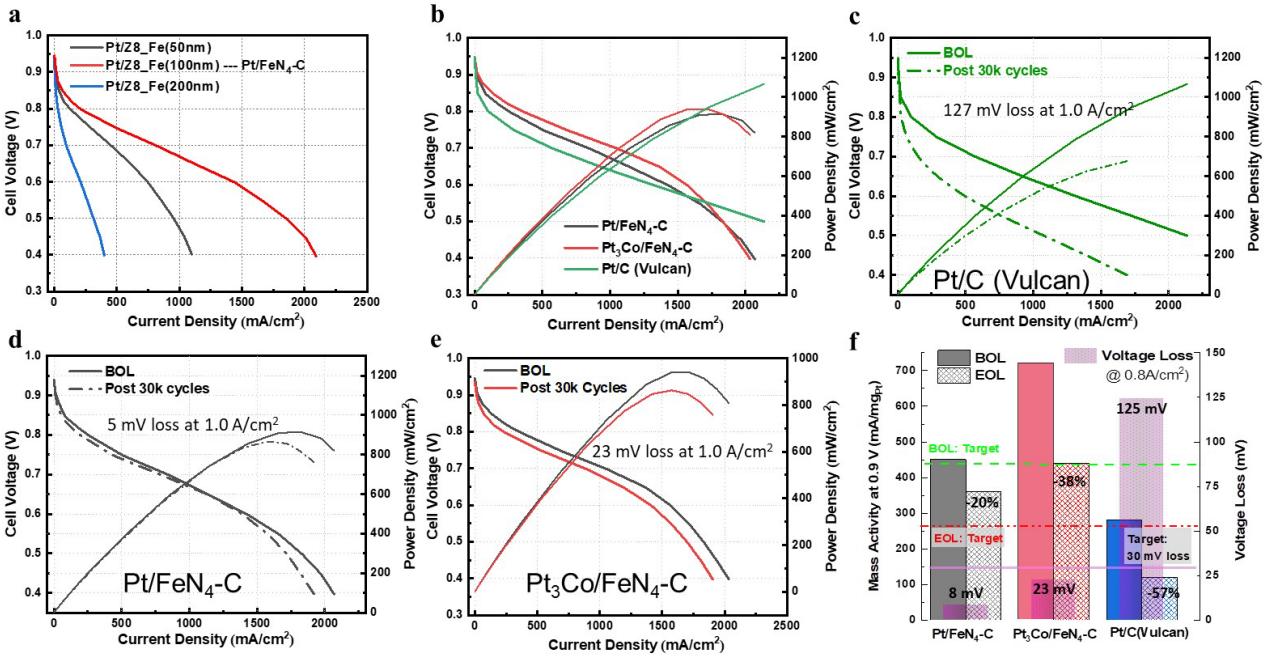

Figure 5. (a) H_2-air fuel cell polarization plots for different Pt catalysts supported on FeN_4-C carbon supports with different sizes. **(b)** H_2-air fuel cell polarization and power density plots for various catalysts supported on the 100 nm FeN_4-C support. BOL and EOL fuel cell polarization and power density plots comparisons during voltage cycles (0.6-0.95V) for (**c**) the Pt/C(XC-72), (**d**) the Pt/FeN_4-C, and (e) the Pt_3Co/FeN_4-C. (**f**) MEA MAs at 0.9 $V_{iR\text{-}free}$ before (solid) and after (hatched) 30k voltage cycles for these studied catalysts; DOE's MA targets for before (green

dashed line, 0.44 A/mg_{Pt}) and after (red dashed line, 0.264 A/mg_{Pt} or 40% of the initial value) AST; Voltage loss at 0.8 A/cm^2 were also indicated with DOE targets for less than 30 mV (solid magenta line).

2.4. Catalyst degradation mechanisms and XAS study

The morphology, structure, and chemical composition of aged FeN_4-C supported PGM catalysts (*i.e.*, after catalyst ASTs for 30,000 voltage cycles) were further studied using advanced electron microscopy and XAS analysis. As shown in **Figure 6a-c**, the Pt NP size and dispersion were well preserved after the AST without apparent agglomeration. These results supported our hypothesis that the existence of FeN_4 sites in supports strengthens the metal-support interaction, leading to less Pt particle detachment and agglomeration. Also, the atomically dispersed FeN_4 sites surrounding the Pt NP are well retained (**Figure S17**). The uniform distribution of Fe and N was further confirmed by using the EDX element mapping (**Figure S18**). It should be noted that the AST for PGM catalyst was performed under H_2/N_2 atmosphere, in which the possible demetallation of FeN_4 sites is insignificant. Notably, the FeN_4-C support used for Pt and Pt_3Co catalysts exhibited significantly enhanced stability during the ORR compared to others.[28] Our previous reports indicated that, after 30, 000 cycles from 0.6 to 1.0 V in O_2 saturated 0.5 M H_2SO_4 solution, the Fe-N-C catalyst only lost 26 mV, and the corresponding STEM/EELS analysis verified the coordination between Fe and N embedded in carbon particles after the AST.[28]

Similarly, the coexistence of FeN_4 sites and Pt_3Co NPs remained in the AST-aged catalysts (**Figure 6d-g**). The ordered intermetallic $L1_2$ Pt_3Co nanostructures with Pt thin skins were nearly unchanged, in good agreement with the observed high durability in MEA testing. However, the catalyst particles are observed to increase the mean diameter. The particle size distributions show tailing toward larger diameters and bi- and tri-modal distributions indicative of particle growth

(**Figure 6h** & **i**). The WAXS data for the aged catalyst from the tested MEAs (**Figure 6j**) shows two peaks for all reflections. One peak overlaps with those observed with the as-prepared catalyst at the two-theta value (**Figure 3f)**. The other shifted to lower two-theta values (yellow arrows in **Figure 6j**) indicates the Co loss by a portion of the catalyst after the AST. The WAXS peaks for the scattering from the (111), (200), (220), and (311) planes were fit with Gaussian peaks. The two-theta values of the centroids of the fit peaks were utilized to calculate lattice spacings, nearest neighbor distances, and mole fractions of Pt and Co in the phases giving rise to the peaks (**Table S3**). The fitting result confirmed a Pt to Co molar ratio in the as-prepared Pt_3Co/FeN_4-C catalyst of 75:25, as expected. Notably, the ordered intermetallic lattice spacing of 40% Pt_3Co NPs in the catalyst was relatively unaffected after the AST. However, the rest of NPs lost nearly all of the original lattice contraction (*i.e.*, lost almost all Co from the lattice), likely due to relatively low ordered structures of Pt_3Co NPs. Therefore, further increasing intermetallic ordered structures is crucial for improving catalyst stability in MEAs.

XAFS spectra were processed and fit with the *Demeter* software package (**Figure S19**).[58] The results for Pt and Co for the Pt/FeN_4-C and Pt_3Co/FeN_4-C catalyst powders and for the cathode catalyst layer of the AST-cycled Pt_3Co/FeN_4-C MEA, are shown in **Tables S4** and **S5**, respectively. The results for a commercial Pt_3Co/C catalyst (TEC 36V32) are also shown for comparison. Pt EXAFS were fit between 1.2 Å and 3.1 Å using Pt-O, Pt-Co, and Pt-Pt scattering paths calculated using *feff* version 6 (*feff6*, Rehr et al.[59]) (**Tables S4)**. For the Pt/FeN_4-C, the large Pt-O coordination number (N_{Pt-O}), as well as the Pt-Pt bond length contraction, indicate that the Pt particles are very small. Regarding the fits for the Pt_3Co catalysts, for intermetallic Pt_3Co, one would observe 4 Co and 8 Pt nearest neighbors around each Pt atom, and 12 Pt and 0 Co around each Co atom. 32% of the Pt-M bonds are Pt-Co in the commercial PtCo alloy standard (TEC 36V32), which is the correct

fraction for a Pt_3Co solid solution. In principle, Pt_3Co intermetallics are expected to have identical Pt-Co and Pt-Pt bond lengths, while traditional solid solutions show different Pt-Pt and Pt-Co lengths. TEC 36V32 Pt_3Co catalyst has Pt-Co and Pt-Pt bond lengths that differ by 0.055 Å, indicating that the Pt_3Co is a solid solution. The results are similar for Pt_3Co/FeN_4-C, with bond lengths that differ by 0.058 Å, although lower N_{Pt-M} indicates a smaller average particle size for this catalyst versus the TEC 36V32. The unexpected fitting results for the Pt_3Co/FeN_4-C catalyst are likely due to the relatively low ordered structures (25% determined by WAXS in Figure 3f) and the possible deformation of crystal lattices. The Pt-O coordination in each case is likely a surface oxide formed by post-synthesis exposure to air. The aged Pt_3Co/FeN_4-C catalyst showed increased N_{Pt-M} and lower N_{Pt-O} coordination numbers than the fresh one, indicating particle growth. It also showed a lower Pt-Co fraction, which suggests significant Co dissociation from Pt. In other words, there is a higher average Pt-Pt coordination in the aged catalysts. Increases in average Pt-Pt bond length, up to +0.039 Å, correspond to larger particles with less cobalt, consistent with the changes in coordination number. It should be noted that Pt EXAFS cannot determine whether these changes are due to the growth of separate Pt-rich particles, loss of Co from the growing Pt_xCo particles, or a rearrangement of the atoms to form a core-shell structure.

Furthermore, the Co K edge EXAFS results are shown in **Table S5**. Significant Co-Co coordination is observed at ~2.63 Å for the Pt_3Co/FeN_4-C, much longer than monometallic Co (R=2.507 Å) and shorter than Pt-Pt (~2.70 Å), offering further evidence of alloying over both intermetallic and a separate class of Co-rich nanoparticles. Thus, a fraction of the particles does consist of intermetallic Pt_3Co, but significant Co is still in a traditional solid-solution alloy within the sensitivity of the EXAFS measurements. In addition, the Pt_3Co/FeN_4-C powder exhibited oxidation of a portion of the Co. Importantly, the Co-M and Co-O coordination numbers are the

same as the Pt-M and Pt-O coordination numbers suggesting that Pt and Co are similarly distributed between the surface and interior of the particles in the as-prepared powder. After the AST-cycled MEA, N_{Co-M} does not increase as much as N_{Pt-M} suggesting that the processes responsible for the change in Co coordination are not in concert with those responsible for the Pt coordination change. One explanation is that a fraction of the Pt-rich particles has increased substantially in size, consistent with the increased average Pt-Pt bond length and the more significant Pt-Pt fraction.

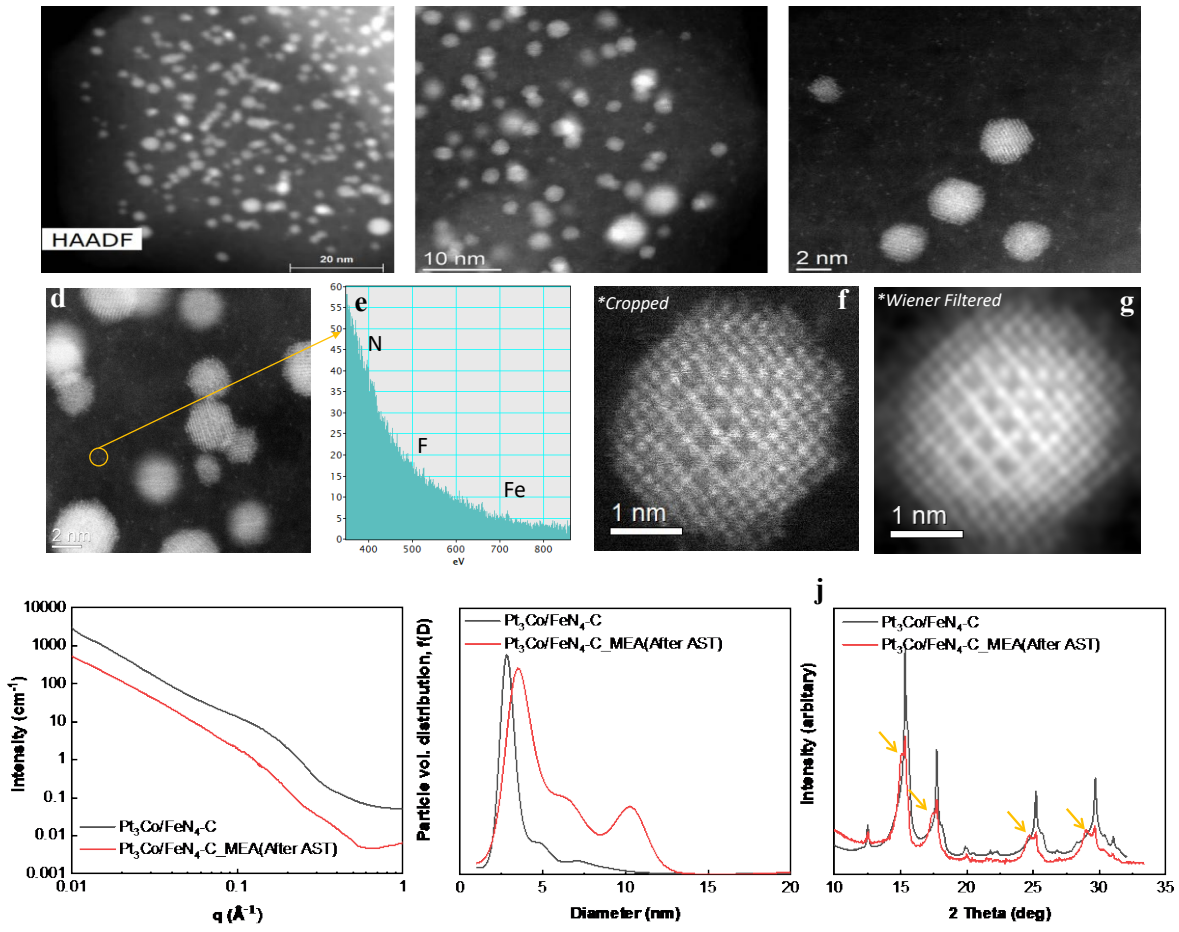

Figure 6. STEM and HAADF-STEM images and EELS analysis of the elemental composition of (**a-c)** the Pt/FeN_4-C catalyst and (**d-g)** the Pt_3Co/FeN_4-C catalysts in MEAs after 30000 voltage cycles (0.6-0.95V) under an H_2/N_2 atmosphere. (**h)** X-ray scattering curves in the SAXS region;

(i) Metal particle volume distributions obtained from SAXS data fits and **(j)** WAXS curves for the Pt_3Co/FeN_4-C before and after 30000 voltage cycles (0.6-0.95 V) in an MEA.

2.5. Theoretical studies of the synergy between FeN_4 sites and Pt

The first-principles density functional theory (DFT) calculations were performed to understand the synergy that MN_4 (M: Fe or Co) and N sites in carbon modify catalytic properties of Pt sites. We constructed a computational model consisting of a thirteen-atom cuboctahedral Pt_{13} cluster and a graphene layer with a FeN_4 (Pt/FeN_4-C), a CoN_4 (Pt/CoN_4-C), an N_4 moiety (Pt/NC), or no dopants (Pt/C). The optimized atomistic structures of Pt/FeN_4-C, Pt/CoN_4-C, Pt/NC, and Pt/C are shown in **Figure 7a** and **Figure S20-21**. We calculated the binding energy using these models, defined as the energy difference between the isolated and the corresponding adsorption systems (*i.e.*, the Pt_{13} cluster and the doped carbon substrate). In **Table S6**, the DFT results show that the binding energies of the Pt/FeN_4-C, Pt/CoN_4-C, Pt/NC, and Pt/C systems are 4.23, 4.15, 3.43, and 2.43 eV, respectively. A more positive value of the binding energy indicates stronger interaction between the Pt cluster and carbon substrates. Consequently, FeN_4 sites in carbon lead to the strongest binding for Pt clusters.

To further distinguish the most favorable binding sites to a Pt NP, we performed the DFT calculations to predict the binding energy of a four-atom tetrahedral Pt_4 cluster adsorbed on various graphene locations containing a FeN_4 moiety (**Figure 7b**). The centroid of a Pt_4 cluster prefers to be anchored on the top of the N site with a binding energy of 3.30 eV, compared to on the Fe site and C site with binding energies of 2.60 and 1.90 eV, respectively. Furthermore, **Figure 7c** shows that when the centroid of a Pt_4 cluster is adsorbed on the N site of a FeN_4 moiety, the Pt atoms in the Pt_4 cluster could form a strong interaction with the central Fe site and the two C sites adjacent

to the N atom. The migration of Pt NPs on carbon leads to catalyst particle agglomeration associated with activity loss.[2] Thus, the calculations predict that a FeN_4 site in carbon could suppress the migration process of Pt NPs, which theoretically elucidated much-enhanced stability of the Pt/FeN_4-C catalyst relative to the Pt/CoN_4-C, Pt/NC, and Pt/C catalysts (**Figure S10**).

Besides, we conducted the DFT calculations to investigate how the FeN_4 site affects the intrinsic ORR activity of Pt sites. Previous studies once indicated that the Pt NP could assist the CoN_4 site to break O-O bond, resulting in the enhancement of the CoN_4 site's ORR activity.[34] Besides, Ao *et al*. suggested that Pt(100) could enhance the ORR activity of FeN_4 active site through tailoring local charge distribution near the FeN_4 site[33]. These studies found that Pt will enhance the ORR activity at MN_4 sites. However, our measured ORR activity on the Pt/FeN_4-C, Pt/CoN_4-C, and Pt/NC catalysts is much higher than PGM-free MN_4 sites (**Figure S22)**. Also, we compared the ORR activity of the Pt/FeN_4-C and the FeN_4-C carbon support at identical loadings (**Figure S23**). Significantly enhanced activity measured with the Pt/FeN_4-C indicates that it is Pt, not FeN_4 sites dominantly contribute to the ORR in the catalyst. Thus, we believe that the opposite effect is more reasonable, *i.e*., FeN_4 sites enhancing the intrinsic activity of Pt sites. As shown in **Figures S24** and **S25**, we constructed FeN_4@Pt(111), CoN_4@Pt(111), and N_4@Pt(111) models consisting of an MN_4 or an N moiety adsorbed at Pt(111) surface. The binding energy of O on the metal surface, *e.g*., Pt(111), denoted as $\Delta E_o - \Delta E_o^{Pt}$, is an adequate descriptor to evaluate the ORR activity.[60] The volcano plot suggests that a metal surface that binds O with about 0.2 eV weaker than Pt(111) surface would have a maximum ORR activity. Here, the binding energies of O on the exposed Pt site of the FeN_4@Pt(111), the CoN_4@Pt(111), and the N_4@Pt(111) were calculated to be 0.15, 0.13, and 0.12 eV weaker (**Figure 7d)**, suggesting that all these PGM-free sites, especially the FeN_4, could effectively enhance the intrinsic activity of the Pt(111) surface. The theoretical

calculations predicted a possible synergy between FeN_4 sites in carbon and the anchored Pt sites for the ORR.

Experimentally, we also verified the possible interaction between FeN_4 sites and Pt. STEM images at the atomic level indicated that Pt nanoparticles coexist with FeN_4 moieties in the immediate vicinity in the Pt/FeN_4-C catalyst, likely generating electronic interactions due to their different electronegativity values. Besides, FeN_4 sites embedded carbon can modify the electronic structure of adjacent carbon. The resultant electron deficiency of carbon likely strengthens the anchored Pt nanoparticle deposition and enhances the metal-support interactions. XPS analysis also confirmed the interaction due to significant positive shifts of Pt 4f peaks in the Pt/FeN_4-C relative to a Pt/C. Therefore, the electron transfer between Pt and FeN_4-rich carbon will likely weaken the O_2/intermediate adsorption on Pt sites with enhanced intrinsic activity.

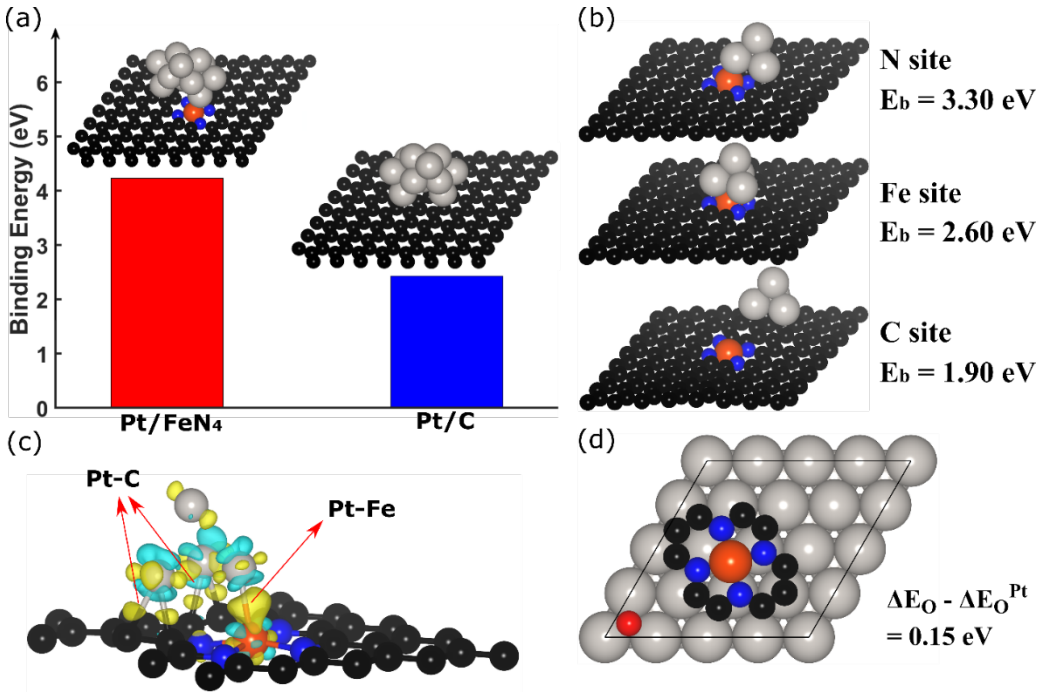

Figure 7. (**a**) Comparison of the calculated binding energies of a thirteen-atom Pt13 cluster adsorbed on a FeN_4 moiety embedded in a graphene layer and an intact graphene layer. (**b**) Optimized atomic structures of a four-atom Pt4 cluster adsorbed on different locations of a FeN_4 moiety embedded in a graphene layer. (**c**) Charge density difference map showing significant charge transfer near Pt-C and Pt-Fe bond. The iso-surface level is 0.01 eV/Å3. Yellow and cyan represent electrons accumulation and depletion, respectively. (**d**) Optimized atomic structure of O adsorption on FeN_4@Pt(111). The active site for ORR is marked with an adsorbed O atom. The black, blue, orange, red, white, and grey balls represent the C, N, Fe, O, H, and Pt atoms, respectively.

Conclusions

In summary, we demonstrated an effective strategy to design high-performance low-PGM fuel cell catalysts by integrating the highly stable Pt_3Co intermetallic nanoparticle and the most promising PGM-free FeN_4 site-rich carbon catalyst. The high surface area, porous morphology, controlled

graphitization degree, and adjustable carbon particle sizes are favorable for Pt and PtCo nanoparticle dispersion with uniform and narrow size distribution. Importantly, the dense FeN_4 sites in carbon support strengthen the interaction between Pt and carbon, thus significantly mitigating nanoparticle agglomeration and enhancing catalyst stability. Theoretical studies predicted that the FeN_4 sites around the Pt sites could weaken the adsorption of O_2 and intermediates by 0.15 eV close to the optimal value (0.20 eV), thus intrinsically improving the catalytic activity of Pt catalysts for the ORR.

We synthesized the atomically dispersed FeN_4 carbon-supported Pt and the ordered cubic $L1_2$ (Pt_3Co) intermetallic catalysts. Compared to the common solid solution A1-structure, PtCo intermetallics with strong Pt-M interaction are particularly promising as new fuel cell catalysts due to their superior M-stabilization in the corrosive ORR conditions. Comprehensive RDE and MEA studies verified that the FeN_4-rich carbon is superior to traditional nitrogen-doped carbon and carbon black concerning ORR activity and stability. In particular, the Pt/FeN_4-C catalyst has achieved compelling activity and stability with 30 mV positive shift in half-wave potential relative to a Pt/C (i.e., Vulcan XC-72) catalyst and only 10 mV loss after 30k potential cycles. MEA performance further demonstrated outstanding mass activity at 0.9 V (0.45 A/mg_{Pt}) and durability (20% loss in MA at 0.9 V and 5 mV loss at 1.0 A/cm^2 MEA studies), achieved the challenging DOE targets by using Pt even without alloying.

The Pt_3Co intermetallic catalyst on the FeN_4-carbon achieved a high ORR activity with half-wave potentials above 0.95 V, representing one of the most active PGM catalysts. The Pt_3Co/FeN_4 MEA reached a power density of 824 mW/cm^2 at 0.67 V and only lost 23 mV at 1.0 A $/cm^2$ after 30,000 voltage cycles in an MEA. Further optimizing electrode structures by optimizing ionomer/carbon ratios can balance ORR mass activity, power density, and durability.

Thus, the effective approach to leveraging the most promising PGM-free FeN_4 sites in the design of ordered PtCo intermetallics for high-performance low-PGM catalysts should be one of new avenues to advance fuel cell catalyst technologies for transportation application. It should be noted that achieving the fully ordered intermetallic alloy structure while maintaining small particle size distribution are crucial for further improving catalyst durability but remains a grand challenge. During the synthesis, higher annealing temperatures and longer treating duration would facilitate the ordered structures but result in significant particle growth. Currently, it is still under debate whether the cubic $L1_2$ (Pt_3Co) or the tetragonal $L1_0$ (PtCo) is more suitable for fuel cell applications concerning activity and stability trade-off.

Conflicts of interest

There are no conflicts to declare.

Acknowledgements

This work was financially supported by the U.S. Department of Energy, Energy Efficiency and Renewable Energy, Hydrogen and Fuel Cell Technologies Office (HFTO) through the Advanced Electro-Catalysts through Crystallographic Enhancement project and by the LANL LDRD program through project 20200200DR. Electron microscopy research was conducted at the Center for Functional Nanomaterials at Brookhaven National Laboratory under Contract DE-SC0012704, DOE Office of Science User Facilities. The authors wish to acknowledge the financial support of the Million Mile Fuel Cell Truck (M2FCT) consortium and Fuel Cell Component R&D Team Lead, Dr. Dimitrios Papageorgopoulos and Program Manager Greg Kleen. The X-ray absorption (MRCAT, 10-BM, and 10-ID) and scattering (XSD, 9-ID-C) experiments were performed at the Advanced Photon Source (APS), a DOE Office of Science User Facility operated for the DOE

Office of Science by Argonne National Laboratory under Contract No. DE-AC02-06CH11357. The operation of MRCAT at the APS is supported by the Department of Energy and the MRCAT member institutions. The submitted manuscript has been created by employees of Triad National Security, LLC, operator of the Los Alamos National Laboratory under Contract No. 89233218CNA000001 with the U.S. Department of Energy, and by UChicago Argonne, LLC, Operator of Argonne National Laboratory under Contract No. DE-AC02-06CH11357. The authors would like to thank Jan Ilavsky and Ivan Kuzmenko of the APS 9-ID-C and Joshua Wright of 10-ID.

References

1. X. Tian, X. F. Lu, B. Y. Xia and X. W. Lou, *Joule*, 2020, **4**, 45-68.
2. J. Hou, M. Yang, C. Ke, G. Wei, C. Priest, Z. Qiao, G. Wu and J. Zhang, *EnergyChem*, 2020, **2**, 100023.
3. Y. Li, H. Wang, C. Priest, S. Li, P. Xu and G. Wu, *Advanced Materials*, 2021, **33**, 2000381.
4. X. X. Wang, M. T. Swihart and G. Wu, *Nature Catalysis*, 2019, **2**, 578-589.
5. Z. Zhao, M. D. Hossain, C. Xu, Z. Lu, Y.-S. Liu, S.-H. Hsieh, I. Lee, W. Gao, J. Yang, B. V. Merinov, W. Xue, Z. Liu, J. Zhou, Z. Luo, X. Pan, F. Zaera, J. Guo, X. Duan, W. A. Goddard and Y. Huang, *Matter*, 2020, **3**, 1774-1790.
6. D. Wang, H. L. Xin, R. Hovden, H. Wang, Y. Yu, D. A. Muller, F. J. DiSalvo and H. D. Abruña, *Nature Materials*, 2013, **12**, 81.
7. X. X. Wang, S. Hwang, Y.-T. Pan, K. Chen, Y. He, S. Karakalos, H. Zhang, J. S. Spendelow, D. Su and G. Wu, *Nano Letters*, 2018, **18**, 4163-4171.
8. C. Chen, Y. Kang, Z. Huo, Z. Zhu, W. Huang, H. L. Xin, J. D. Snyder, D. Li, J. A. Herron and M. Mavrikakis, *Science*, 2014, **343**, 1339-1343.

9. M. Li, Z. Zhao, T. Cheng, A. Fortunelli, C.-Y. Chen, R. Yu, Q. Zhang, L. Gu, B. V. Merinov and Z. Lin, *Science*, 2016, **354**, 1414-1419.

10. X. Huang, Z. Zhao, L. Cao, Y. Chen, E. Zhu, Z. Lin, M. Li, A. Yan, A. Zettl and Y. M. Wang, *Science*, 2015, **348**, 1230-1234.

11. C. Cui, L. Gan, M. Heggen, S. Rudi and P. Strasser, *Nature Materials*, 2013, **12**, 765-771.

12. X. Tian, X. Zhao, Y.-Q. Su, L. Wang, H. Wang, D. Dang, B. Chi, H. Liu, E. J. M. Hensen, X. W. Lou and B. Y. Xia, *Science*, 2019, **366**, 850-856.

13. H. Zhu, S. Zhang, D. Su, G. Jiang and S. Sun, *Small*, 2015, **11**, 3545-3549.

14. C. Wang, Y. Hou, J. Kim and S. Sun, *Angew. Chem. Int. Ed.*, 2007, **46**, 6333-6335.

15. Y. Bing, H. Liu, L. Zhang, D. Ghosh and J. Zhang, *Chemical Society Reviews*, 2010, **39**, 2184-2202.

16. J. Liang, F. Ma, S. Hwang, X. Wang, J. Sokolowski, Q. Li, G. Wu and D. Su, *Joule*, 2019.

17. W. Xia, A. Mahmood, Z. Liang, R. Zou and S. Guo, *Angew. Chem. Int. Ed.*, 2016, **55**, 2650-2676.

18. C. Wang and J. S. Spendelow, *Current Opinion in Electrochemistry*, 2021, **28**, 100715.

19. Q. Li, L. Wu, G. Wu, D. Su, H. Lv, S. Zhang, W. Zhu, A. Casimir, H. Zhu, A. Mendoza-Garcia and S. Sun, *Nano Letters*, 2015, **15**, 2468-2473.

20. J. Liang, N. Li, Z. Zhao, L. Ma, X. Wang, S. Li, X. Liu, T. Wang, Y. Du, G. Lu, J. Han, Y. Huang, D. Su and Q. Li, *Angew. Chem. Int. Ed.*, 2019, **131**, 15617-15623.

21. J. Li, S. Sharma, X. Liu, Y.-T. Pan, J. S. Spendelow, M. Chi, Y. Jia, P. Zhang, D. A. Cullen and Z. Xi, *Joule*, 2019, **3**, 124-135.

22. G. Wu, K. L. More, C. M. Johnston and P. Zelenay, *Science*, 2011, **332**, 443-447.

23. H. T. Chung, D. A. Cullen, D. Higgins, B. T. Sneed, E. F. Holby, K. L. More and P. Zelenay, *Science*, 2017, **357**, 479-484.

24. Q. Shi, S. Hwang, H. Yang, F. Ismail, D. Su, D. Higgins and G. Wu, *Materials Today*, 2020, **37**, 93-111.

25. Y. Zhu, J. Sokolowski, X. Song, Y. He, Y. Mei and G. Wu, *Advanced Energy Materials*, 2020, **10**, 1902844.

26. Y. Wang, H. Su, Y. He, L. Li, S. Zhu, H. Shen, P. Xie, X. Fu, G. Zhou, C. Feng, D. Zhao, F. Xiao, X. Zhu, Y. Zeng, M. Shao, S. Chen, G. Wu, J. Zeng and C. Wang, *Chemical Reviews*, 2020, **120**, 12217-12314.

27. H. Zhang, S. Hwang, M. Wang, Z. Feng, S. Karakalos, L. Luo, Z. Qiao, X. Xie, C. Wang and D. Su, *Journal of the American Chemical Society*, 2017, **139**, 14143-14149.

28. H. Zhang, H. T. Chung, D. A. Cullen, S. Wagner, U. I. Kramm, K. L. More, P. Zelenay and G. Wu, *Energy & Environmental Science*, 2019, **12**, 2548-2558.

29. Q. Shi, Y. He, X. Bai, M. Wang, D. A. Cullen, M. Lucero, X. Zhao, K. L. More, H. Zhou, Z. Feng, Y. Liu and G. Wu, *Energy & Environmental Science*, 2020, **13**, 3544-3555.

30. S. T. Thompson and D. Papageorgopoulos, *Nature Catalysis*, 2019, **2**, 558-561.

31. G. Wu, D. Li, C. Dai, D. Wang and N. Li, *Langmuir*, 2008, **24**, 3566-3575.

32. G. Wu, C. Dai, D. Wang, D. Li and N. Li, *Journal of Materials Chemistry*, 2010, **20**, 3059-3068.

33. X. Ao, W. Zhang, B. Zhao, Y. Ding, G. Nam, L. Soule, A. Abdelhafiz, C. Wang and M. Liu, *Energy & Environmental Science*, 2020, **13**, 3032-3040.

34. L. Chong, J. Wen, J. Kubal, F. G. Sen, J. Zou, J. Greeley, M. Chan, H. Barkholtz, W. Ding and D.-J. Liu, *Science*, 2018, **362**, 1276-1281.

35. Y. He, S. Liu, C. Priest, Q. Shi and G. Wu, *Chemical Society Reviews*, 2020, **49**, 3484-3524.

36. Z. Qiao, S. Hwang, X. Li, C. Wang, W. Samarakoon, S. Karakalos, D. Li, M. Chen, Y. He and M. Wang, *Energy & Environmental Science*, 2019, **12**, 2830-2841.

37. Z. Qiao, H. Zhang, S. Karakalos, S. Hwang, J. Xue, M. Chen, D. Su and G. Wu, *Applied Catalysis B: Environmental*, 2017, **219**, 629-639.

38. P. G. Santori, F. D. Speck, J. Li, A. Zitolo, Q. Jia, S. Mukerjee, S. Cherevko and F. Jaouen, *Journal of The Electrochemical Society*, 2019, **166**, F3311.

39. J. Li, H. Zhang, W. Samarakoon, W. Shan, D. A. Cullen, S. Karakalos, M. Chen, D. Gu, K. L. More, G. Wang, Z. Feng, Z. Wang and G. Wu, *Angew. Chem. Int. Ed.*, 2019, **58**, 18971-18980.

40. S. Liu, M. Wang, X. Yang, Q. Shi, Z. Qiao, M. Lucero, Q. Ma, K. L. More, D. A. Cullen, Z. Feng and G. Wu, *Angew. Chem. Int. Ed.*, 2020, **59**, 21698-21705.

41. X. Zhao, X. Yang, M. Wang, S. Hwang, S. Karakalos, M. Chen, Z. Qiao, L. Wang, B. Liu, Q. Ma, D. A. Cullen, D. Su, H. Yang, H.-Y. Zang, Z. Feng and G. Wu, *Applied Catalysis B: Environmental*, 2020, **279**, 119400.

42. K. Sato, K. Yanajima and T. J. Konno, *Journal of Nanomaterials*, 2013, **2013**.

43. Y. Chen, J. Wang, H. Liu, R. Li, X. Sun, S. Ye and S. Knights, *Electrochemistry Communications*, 2009, **11**, 2071-2076.

44. L. Qiu, F. Liu, L. Zhao, W. Yang and J. Yao, *Langmuir*, 2006, **22**, 4480-4482.

45. X. Zhang, H. Wang, J. Key, V. Linkov, S. Ji, X. Wang, Z. Lei and R. Wang, *Journal of the Electrochemical Society*, 2012, **159**, B270.

46. B. Y. Xia, H. B. Wu, N. Li, Y. Yan, X. W. Lou and X. Wang, *Angew. Chem. Int. Ed.*, 2015, **54**, 3797-3801.

47. S. Axnanda, K. Cummins, T. He, D. Goodman and M. Soriaga, *ChemPhysChem*, 2010, **11**, 1468-1475.

48. Y. He, Q. Shi, W. Shan, X. Li, A. J. Kropf, E. C. Wegener, J. Wright, S. Karakalos, D. Su, D. A. Cullen, G. Wang, D. J. Myers and G. Wu, *Angew. Chem. Int. Ed.*, 2021, **60**, 9516-9526.

49. Y. He, H. Guo, S. Hwang, X. Yang, Z. He, J. Braaten, S. Karakalos, W. Shan, M. Wang, H. Zhou, Z. Feng, K. L. More, G. Wang, D. Su, D. A. Cullen, L. Fei, S. Litster and G. Wu, *Advanced Materials*, 2020, **32**, 2003577.

50. Y. He, S. Hwang, D. A. Cullen, M. A. Uddin, L. Langhorst, B. Li, S. Karakalos, A. J. Kropf, E. C. Wegener, J. Sokolowski, M. Chen, D. Myers, D. Su, K. L. More, G. Wang, S. Litster and G. Wu, *Energy & Environmental Science*, 2019, **12**, 250-260.

51. X. X. Wang, D. A. Cullen, Y. T. Pan, S. Hwang, M. Wang, Z. Feng, J. Wang, M. H. Engelhard, H. Zhang, Y. He, Y. Shao, D. Su, K. More, J. Spendelow and G. Wu, *Advanced Materials*, 2018, **30**, 1706758.

52. Y. Xiong, Y. Yang, H. Joress, E. Padgett, U. Gupta, V. Yarlagadda, D. N. Agyeman-Budu, X. Huang, T. E. Moylan and R. Zeng, *Proceedings of the National Academy of Sciences*, 2019, **116**, 1974-1983.

53. S. Kraft, J. Stümpel, P. Becker and U. Kuetgens, *Review of scientific instruments*, 1996, **67**, 681-687.

54. R. L. Borup, A. Kusoglu, K. C. Neyerlin, R. Mukundan, R. K. Ahluwalia, D. A. Cullen, K. L. More, A. Z. Weber and D. J. Myers, *Current Opinion in Electrochemistry*, 2020, **21**, 192-200.

55. T. R. Garrick, T. E. Moylan, M. K. Carpenter and A. Kongkanand, *Journal of The Electrochemical Society*, 2016, **164**, F55-F59.

56. A. Uddin, L. Dunsmore, H. Zhang, L. Hu, G. Wu and S. Litster, *ACS Appl. Mater. Interfaces*, 2019, **12**, 2216-2224.

57. S. Lee, J.-H. Jang, I. Jang, D. Choi, K.-S. Lee, D. Ahn, Y. S. Kang, H.-Y. Park and S. J. Yoo, *Journal of Catalysis*, 2019, **379**, 112-120.

58. B. Ravel and M. Newville, *Journal of Synchrotron Radiation*, 2005, **12**, 537-541.

59. J. Rehr, R. Albers and S. Zabinsky, *Physical review letters*, 1992, **69**, 3397.

60. J. Greeley, I. E. L. Stephens, A. S. Bondarenko, T. P. Johansson, H. A. Hansen, T. F. Jaramillo, J. Rossmeisl, I. Chorkendorff and J. K. Nørskov, *Nature Chemistry*, 2009, **1**, 552-556.